Thin–Walled Structures 212 (2025) 113127

Contents lists available at ScienceDirect

Thin-Walled Structures

journal homepage: www.elsevier.com/locate/tws

Analysis and design of Kirigami-based metallic energy-dissipating systems

Sahand Khalilzadehtabrizi [a], Iman Mohagheghian [a], Martin G. Walker [b,*]

[a] School of Engineering, University of Surrey, Stag Hill, University Campus, Guildford, GU2 7XH, Surrey, United Kingdom
[b] Department of Engineering, Durham University, Lower Mount Joy, South Road, Durham, DH1 3LE, United Kingdom

ARTICLE INFO

Keywords:
Kirigami
Kinematic analysis
Energy dissipating
Yield line analysis
Metallic Kirigami
Fall arrest

ABSTRACT

Kirigami, the Japanese art of paper cutting, can be used to generate complex 3D shapes from 2D sheets. Kirigami structures can also be highly stretchable and accommodate extremely large strains from common materials, such as aluminium, which allow relatively small strains at failure. The high stretchability of Kirigami makes it an ideal method for energy dissipation applications. This study investigates the mechanics and energy-dissipating behaviour of Kirigami made from metallic materials. A comprehensive analysis is conducted using a combination of reduced-order analytical modelling, finite element analysis, and experimental validation. The analytical model is used to produce a design methodology for energy-dissipating devices based on metallic ribbon Kirigami and is then applied as a case study to the design of a novel fall arrest system. The results of this study will enable the design of efficient, and highly customisable energy-dissipating systems based on metallic Kirigami.

1. Introduction

Kirigami is a Japanese art form derived from the words "kiri" (cut) and "kami" (paper). It involves cutting to create elaborate designs. Kirigami structures demonstrate extraordinary stretchability and are capable of undergoing extensive deformation and in-plane strains through out-of-plane buckling [1]. This distinctive feature makes Kirigami a versatile and widely applicable technique in fields such as architecture, engineering, and material science.

Kirigami encompasses a wide variety of cutting patterns, further expanding its applicability and design possibilities. Kirigami cutting patterns can be broadly classified [2] into those created solely by cutting such as fractal cut [3,4] and ribbon [1,5], and those formed by both cutting and folding such as lattice [6,7], zigzag [8], and closed-loop Kirigami [9–11].

The versatility of kirigami has led to applications in a wide range of fields including wearable sensors [12–14], soft robotics [15,16], adaptive facades [17,18], fog harvesting [19], and solar tracking [20,21]. Kirigami has also shown promise as the basis of energy-dissipating devices. Examples include the axial crushing of Kirigami tubes [22–24], the crushing of Kirigami-based sandwich panel cores [25–27], and protective wrapping [23]. Studies have also used Kirigami to address challenges such as high initial peak force and fluctuating crushing resistance, aiming to improve the stability and efficiency of these structures under impact loads [25,27]. However, to date studies have centred on devices designed to withstand compression or shear forces, reflecting a common focus in energy absorber research [26].

This study investigates the tensile energy-dissipating behaviour of ribbon Kirigami constructed from metallic materials using a combination of analytical, experimental, and numerical approaches. Energy is dissipated through plastic deformations concentrated in discrete yield lines which emerge due to out-of-plane deformation. The analytical model forms the basis of a design methodology which is then applied as a case study to the design of a novel fall arrest system. Metallic Kirigami offers a simple, and highly customisable, method of constructing novel energy dissipating devices.

2. Geometry and experiments

The ribbon Kirigami cut pattern comprises an array of parallel cuts arranged into columns and rows, as shown in Fig. 1(a). The region surrounding each cut is identical forming a unit cell, shown in Fig. 1(b), which repeats throughout the sheet. The number of unit cells along the height is n_y and across the width is n_x. The width of each unit cell is L and the link widths are w_h. The vertical space between two consecutive cutting rows is L_y and L_x is the length of each cut. The thickness of the sheet is t_s.

Ribbon kirigami can buckle out-of-plane into two distinct modes: symmetric and anti-symmetric depending on the cut pattern [5]. The large stretchability of the anti-symmetric mode makes it ideal for use as the basis of energy-dissipating devices. This study exclusively uses cut patterns which ensure the anti-symmetric mode will occur.

* Corresponding author.
E-mail address: martin.g.walker@durham.ac.uk (M.G. Walker).

https://doi.org/10.1016/j.tws.2025.113127
Received 30 October 2024; Received in revised form 21 February 2025; Accepted 25 February 2025
Available online 7 March 2025

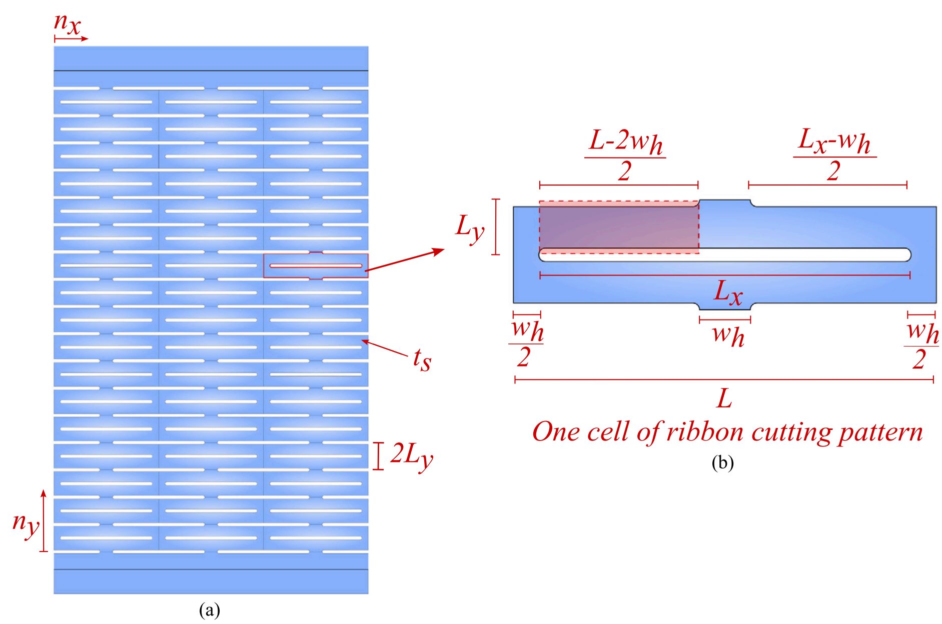

Fig. 1. (a) Geometry of the ribbon cutting pattern and (b) The ribbon Kirigami unit cell. Half the aspect ratio of the shaded facet, $\psi = L_y/(L - w_h)$, is a key parameter for the behaviour of metallic ribbon Kirigami.

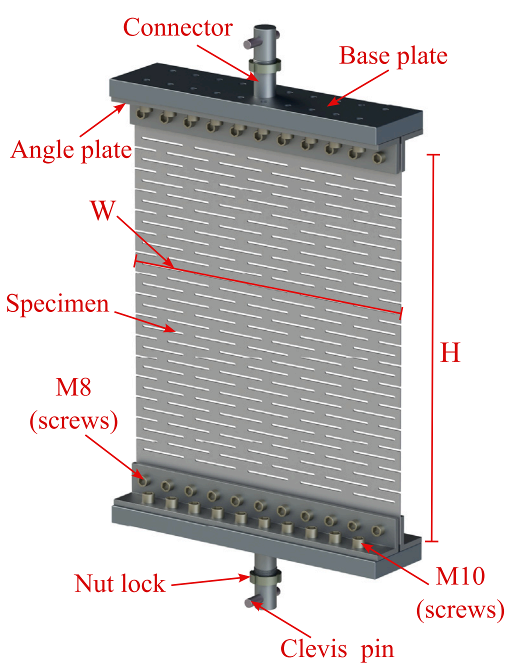

Fig. 2. Schematic of experimental setup, H and W are symbols of the entire height and width of specimen.

A set of two Kirigami specimens with identical geometrical parameters ($L = 60$ mm, $w_h = 5$ mm, $L_y = 5$ mm, $n_y = 10$, $n_x = 2$, and $t_s = 1$ mm) were fabricated to provide experimental validation. 1060 Aluminium alloy sheet was used and the test specimens were manufactured by water jet cutting, which avoids the creation of heat-affected zones that occur when laser or plasma cutting is used.

A test fixture was designed to securely grip the top and bottom edges of the Kirigami, as shown in Fig. 2. The test fixture was connected to an Instron 2580 universal testing machine. Both ends of the kirigami were securely fixed to the test fixtures and the top grip moved upwards under displacement control at a rate of 10 mm/min.

In Fig. 3, the deformed shapes of the ribbon Kirigami in both experiment and finite element analysis (Section 3) are showcased, revealing a high degree of similarity. The cells located in the middle rows started buckling first due to the influence of the fixed boundary conditions provided by grips. Then further rows buckled sequentially moving outwards from the initially buckled cells.

The force–displacement behaviour of the experiments and finite element analysis is depicted in Fig. 4 showing very good agreement. Initially, the force increases rapidly to a peak value before out of plane buckling occurs. At the onset of out-of-plane buckling, the force drops rapidly to a nearly constant post-buckling plateau. This post-buckling plateau force, in particular, is crucial for energy-dissipating purposes.

The observed force oscillations are the result of the buckling of sequential rows of the sheet. At high displacements the force increases rapidly since a kinematic limit of extension is reached and in-plane stretching of the sheet becomes increasingly significant, eventually leading to failure by tearing.

3. Finite element analysis

Finite element simulations using ABAQUS [28] were conducted to complement the experiments. The entire structure is meshed using four-node quadrilateral shell elements with reduced integration (S4R). A mesh sensitivity analysis was conducted using three different mesh sizes: 0.1 mm, 0.25 mm, and 0.5 mm, as shown in Fig. 5. The corresponding force–displacement graphs are presented in Fig. 6. The results indicate that increasing the mesh size up to 0.5 mm does not produce any significant changes to the response. Therefore, a mesh size of 0.5 mm was used for the finite element analysis.

The Johnson-Cook plasticity material model [29] with isotropic strain hardening was employed with the parameters for 1060 aluminium alloy shown in Table 1. To obtain the parameters, the values outlined in [30] were initially employed to construct a finite element model of tensile coupon specimens. The material model parameters were then adjusted to match experimental tensile coupon tests on the same aluminium sheet used to manufacture the test specimens.

All six degrees of freedom were constrained at the bottom grip. For the top grip, all degrees of freedom except displacement in the extension direction were constrained. Initially, an eigenvalue buckling analysis was performed. Deformations from the first twenty buckling

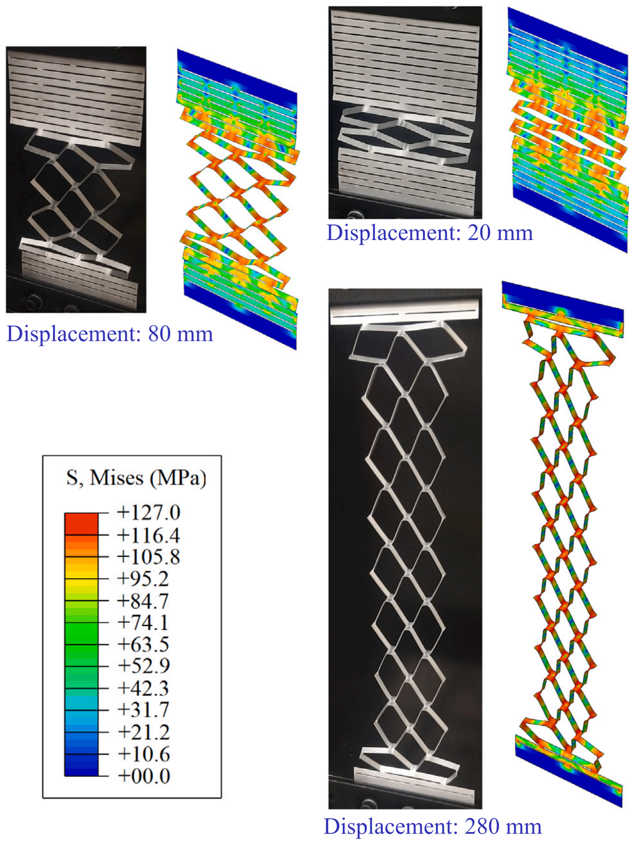

Fig. 3. The post-buckled shape of ribbon Kirigami, in the anti-symmetric mode, is shown for both experiment and finite element analysis. The three different deformation states (20 mm, 80 mm, and 280 mm) show excellent qualitative agreement.

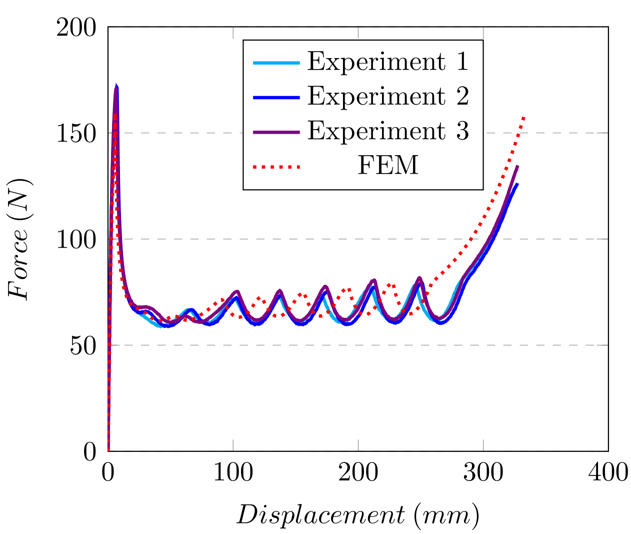

Fig. 4. Force–Displacement graphs of experimental tests and finite element analysis showing very good agreement. The force oscillations observed are a result of the buckling of sequential rows of the sheet.

modes were scaled by 0.025, summed, and imposed as initial imperfections for the subsequent non-linear static analysis step. The simulation proceeded under displacement control of the top edge of the sheet. Comparison of the force–displacement behaviour to experiments in Fig. 4 shows very good agreement. The difference between the average plateau force in the experiments and finite element analysis is less than 2%.

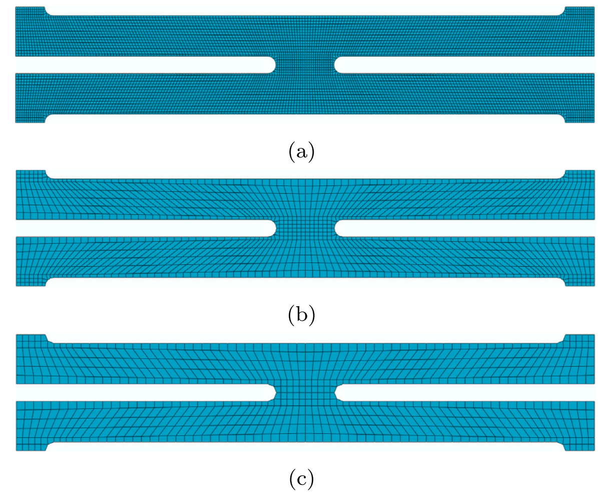

Fig. 5. Unit cell mesh with element sizes of (a) 0.1 mm, (b) 0.25 mm, and (c) 0.5 mm was used to analyse the mesh size sensitivity.

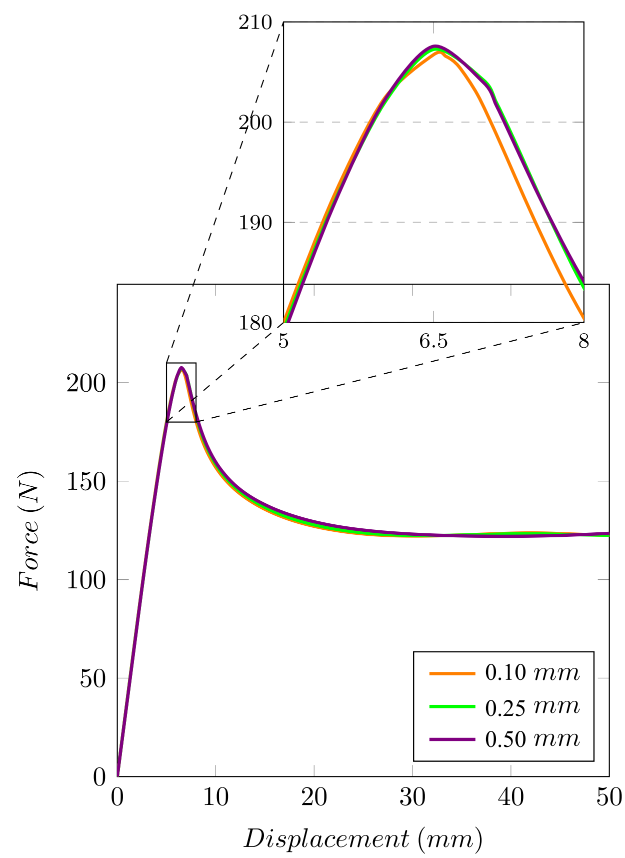

Fig. 6. Force–displacement graphs for different mesh sizes (0.1 mm, 0.25 mm, and 0.5 mm). The results demonstrate that increasing the mesh size up to 0.5 mm has no significant impact on the force–displacement behaviour.

4. Analytical model

An analytical characterisation of the response allows a deeper understanding of observed behaviour and provides a simple means to design energy dissipating systems using Kirigami. We make use of yield-line mechanism analysis, a technique widely used to study the collapse of thin-walled structures [31], to investigate the post-buckling

Table 1
Material properties and Johnson–Cook parameters of 1060 aluminium alloy.

Material properties	
Density, ρ (ton/mm^3)	2.7×10^{-9}
Young's modulus, E (MPa)	68 000
Poisson's ratio, ν	0.33
Johnson–Cook model parameters	
A (MPa)	88
B (MPa)	45
n	0.15
m	0.0
C	0.001
$\dot{\varepsilon}_0$ (s^{-1})	1.0

behaviour and predict the energy absorption capacity. To utilise yield-line analysis, we begin by developing a kinematic model of a unit cell for the anti-symmetric buckling mode. The unit cell analysis is then extended to describe the global response by making use of the so called 'Maxwell Construction' [32,33]. The analytical treatment of a unit cell which is then used to predict global mechanical behaviour is common for kirigami structures like ours [1,5,16]. It is also a common approach for cellular structures more generally [34].

4.1. Unit cell analysis

To conduct an analysis of the ribbon Kirigami structure we first focus on one unit cell (Fig. 7). The analysis assumes that the unit cell can be represented as a series of rigid facets connected by revolute hinges, shown as dashed lines in Fig. 7. A consequence of this assumption is that no elastic in-plane pre-buckling deformation is possible [35]. The axial strain of a unit cell is defined as the unit cell displacement (δ) divided by the height of the undeformed unit cell ($2L_y$) [20]:

$$\varepsilon = \frac{\delta}{2L_y} = \frac{1}{\cos\theta} - 1 \tag{1}$$

Eq. (1) can be inverted to write the angle θ in terms of the strain:

$$\theta = \cos^{-1}\left(\frac{1}{1+\varepsilon}\right) \tag{2}$$

where the rotation angle, θ, is illustrated in Fig. 7(b), and ε is the axial strain. The folding angle of the hinges, represented as β in Fig. 7(b), is obtained from the geometry of the deformed unit cell (Fig. 7(b)) [20]:

$$\beta = \sin^{-1}\left[\frac{2L_y \tan\theta}{L_x - w_h}\right] \tag{3}$$

For the purposes of this analysis, we assume a rigid-perfectly plastic material with a hinge plastic moment resistance of [31]:

$$M_p = \frac{f_y \cdot L_y \cdot t_s^2}{4} \tag{4}$$

where L_y represents the width of the plastic hinge (see Fig. 7), f_y is the yield stress of the base material, and t_s is the thickness of the sheet. As depicted by dotted lines in Fig. 7(a), each unit cell consists of eight yield lines. Hence, the plastic strain energy required to stretch a single unit cell is:

$$U_s = 8 \cdot M_p \cdot \beta = 2 f_y L_y t_s^2 \sin^{-1}\left(2\psi\sqrt{\varepsilon(\varepsilon+2)}\right) \tag{5}$$

where $\psi = L_y/(L_x - w_h) = L_y/(L - 2w_h)$ is half the aspect ratio of the rigid facets, see the red shaded box in Fig. 1(b). To reasonably achieve anti-symmetric deformation, the conditions $(L - w_h)/L_y > 3$ and $(L - w_h)/w_h > 2$ must be satisfied [5]. This leads to the constraint: $0 < \psi < 2/3$.

To determine the force required to stretch the unit cell as a function of displacement δ, the principle of stationary total potential energy is used. The total potential energy of the system is:

$$\Pi = U_s - F\delta \tag{6}$$

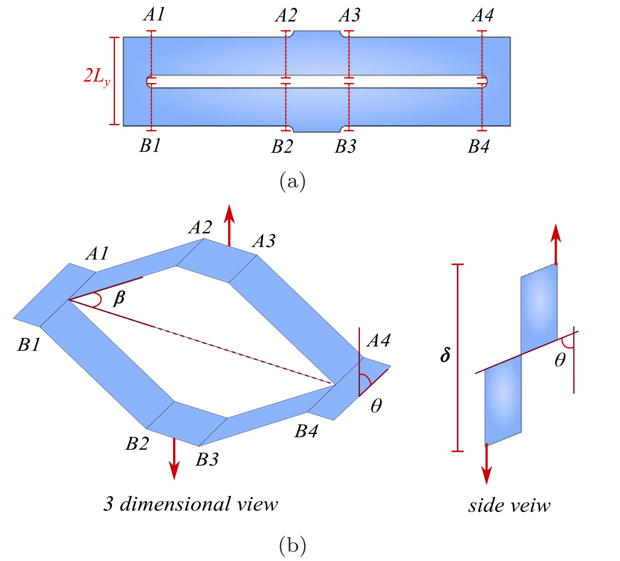

Fig. 7. A unit cell (a) consists of eight plastic hinge lines (A1–A4, B1–B4). The idealised three-dimensional deformed shape (b) in the anti-symmetric mode shows the hinge rotations, β, and unit cell rotation angle, θ (Fig. 9).

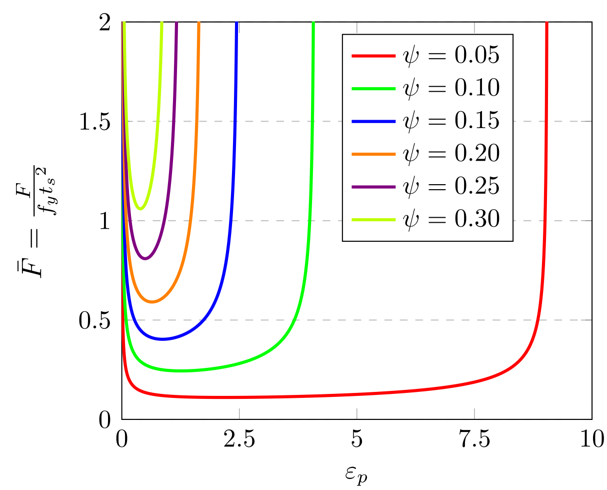

Fig. 8. Dimensionless force, $\bar{F}$, vs. strain, ε, behaviour for $0.05 \le \psi \le 0.30$.

where F is the force and δ is the extension of the unit cell. For equilibrium $d\Pi/d\delta = 0$ and the dimensionless extension force is:

$$\bar{F} = \frac{F}{f_y {t_s}^2} = \frac{1}{f_y {t_s}^2}\frac{dU_s}{d\delta} = \frac{2(\varepsilon+1)\psi}{\sqrt{\varepsilon(\varepsilon+2)\left(1 - 4\varepsilon(\varepsilon+2)\psi^2\right)}} \tag{7}$$

Fig. 8 shows plots of the dimensionless force ($\bar{F}$) vs strain (ε) for a single unit cell with different values of ψ. The minimum force decreases with decreasing ψ. By setting the denominator of Eq. (7) equal to zero, the maximum strain can be computed as:

$$\varepsilon_{max} = \frac{\sqrt{4\psi^2+1}}{2\psi} - 1 \tag{8}$$

The unit cell analysis is now extended to the Kirigami sheet.

4.2. Analysis of the Kirigami sheet

Fig. 9 illustrates the global buckling process of a single column Kirigami structure consisting of a chain of identical unit cells. When subjected to in-plane extension perpendicular to the cuts, Δ, initially the cuts open slightly while remaining in plane (Fig. 9a). After a

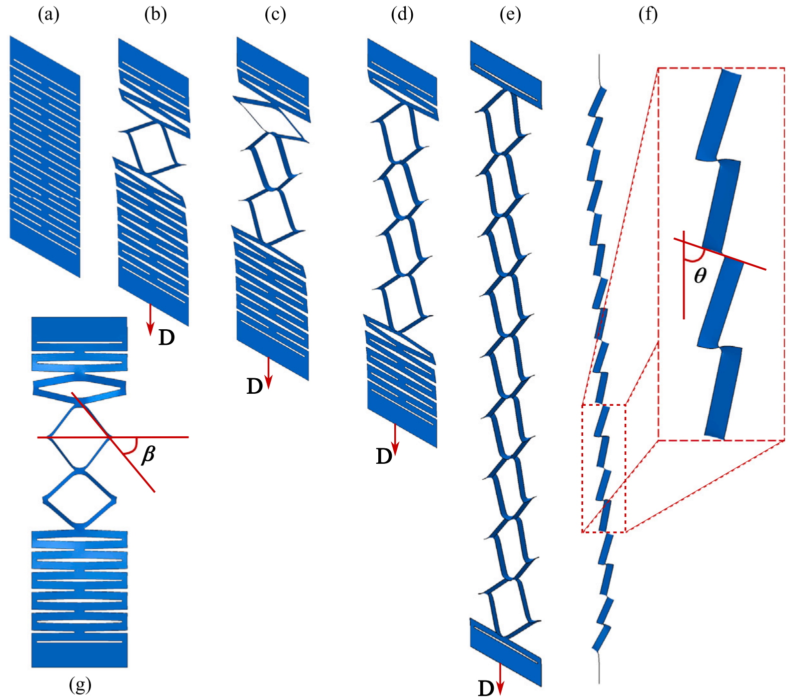

Fig. 9. Schematic diagram illustrating the extension process of ribbon Kirigami in the anti-symmetric buckling mode. The deformation sequence begins with in plane deformation (a), at a critical deformation a row buckles out of plane (b), followed by successive rows buckling (c–d). Eventually, the Kirigami is fully stretched and all rows have buckled out of plane (e). (f) shows a side view of a fully stretched Kirigami with the unit cell rotation angle, θ, while (g) shows the folding angle of the hinges, β.

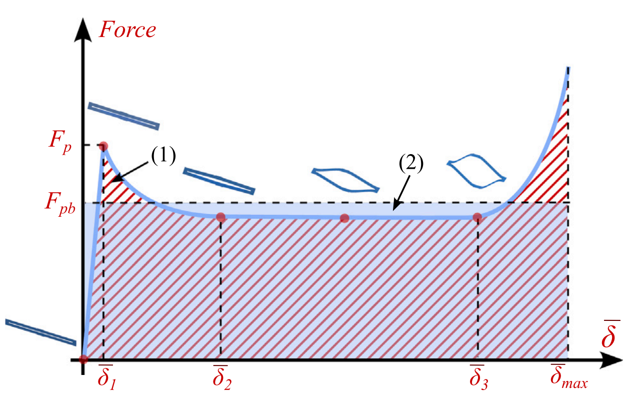

Fig. 10. Schematic force–displacement graph of a single unit cell. F_{pb} is the force required to propagate the deformation. It is obtained by ensuring the red hashed area (1) and the blue shaded area (2) are equal.

critical extension is reached, one row of cuts buckles out-of-plane (Fig. 9b). Due to the boundary constraints at the top and bottom, this buckling typically starts in the middle rows. As extension continues, the deformation leads to the out-of-plane buckling of successive rows (Fig. 9c-d). Finally, when all of the rows are deformed, the entire specimen begins stretching together, with all cells assuming a similar deformed shape, as shown in Fig. 9e.

The force–displacement behaviour of a unit cell is shown schematically in Fig. 10. The up-down-up force–displacement behaviour is indicative of a propagating instability phenomenon [36]. According to the Maxwell construction [32,33] the force required to propagate the unit cell deformation along the length of the sheet, F_{pb}, is obtained by ensuring the area below the force–displacement curve, as shown by the red dashed area (1) in Fig. 10, is equal to that below the constant F_{pb}, as shown by the blue shaded area (2) in Fig. 10. The propagation force (Maxwell load), F_{pb}, is therefore obtained by computing the integral

$$\int_0^{\delta_{\max}} \left(F - F_{pb}\right) d\delta = \int_0^{\epsilon_{\max}} \left(\bar{F} - \bar{F}_{pb}\right) d\epsilon = 0 \tag{9}$$

Solving for the dimensionless propagation force, $\bar{F}_{pb}$:

$$\bar{F}_{pb} = \frac{F_{pb}}{f_y t_s{}^2} = \pi\psi\left(2\psi + \sqrt{1+4\psi^2}\right) \tag{10}$$

where the small elastic region ($\delta < \delta_1$) has been neglected to simplify the calculation. We assume the propagation load computed using Eq. (10) scales linearly with the number of unit cells in parallel, n_x. Therefore the global force to propagate deformation along a ribbon Kirigami sheet is:

$$F_g = n_x F_{pb} \longrightarrow \bar{F}_g = \frac{\bar{F}_{pb}}{n_x} = \frac{F_{pb}}{n_x f_y t_s^2} \tag{11}$$

Fig. 11 shows a schematic force–displacement graph of the global ribbon Kirigami under tensile load in the anti-symmetric buckling mode (see Fig. 3). This looks qualitatively similar to the force–displacement behaviour of the unit cell, shown in Fig. 10. However, the plateau region (between Δ_2 and Δ_3) has a force equal to $F_g = n_x F_{pb}$. The peak force, F_p, is highly imperfection sensitive and we therefore do not attempt to compute this.

Conducting an experiment, or finite element analysis, of a single unit-cell is not feasible due to the influence of boundary conditions. This issue is evident from Fig. 3. Notice that the top/bottom of each unit cell rotates during deformation. It would be extremely difficult to accurately replicate these boundary conditions experimentally, or in finite element analysis, and would require making assumptions about the evolution of the boundary conditions which would have a significant influence on the results. Therefore, we compare analytical model predictions of global mechanical behaviour with the results of finite element analysis.

Fig. 12(a) compares the finite element results with the propagation load, F_g, demonstrating good agreement. A large finite element parametric study was performed with geometries spanning $\psi = 0.04$

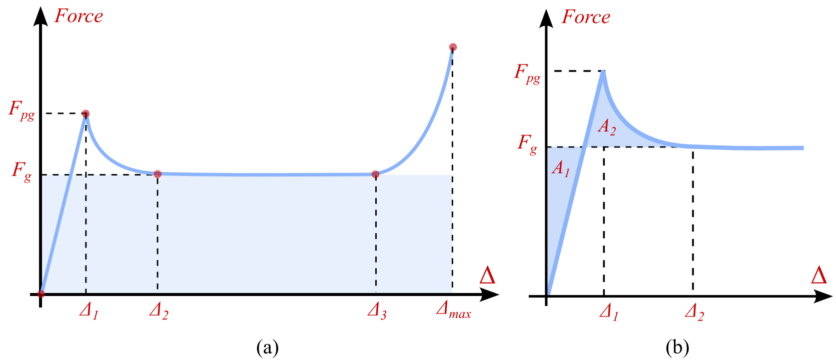

Fig. 11. (a) Schematic of a typical Force–Displacement graph depicting the behaviour of ribbon Kirigami under tensile load. The plateau force $F_g = n_x F_{pb}$. (b) Assuming $A_1 \geq A_2$ leaves the shaded area in (a) as a lower bound on the total energy dissipated.

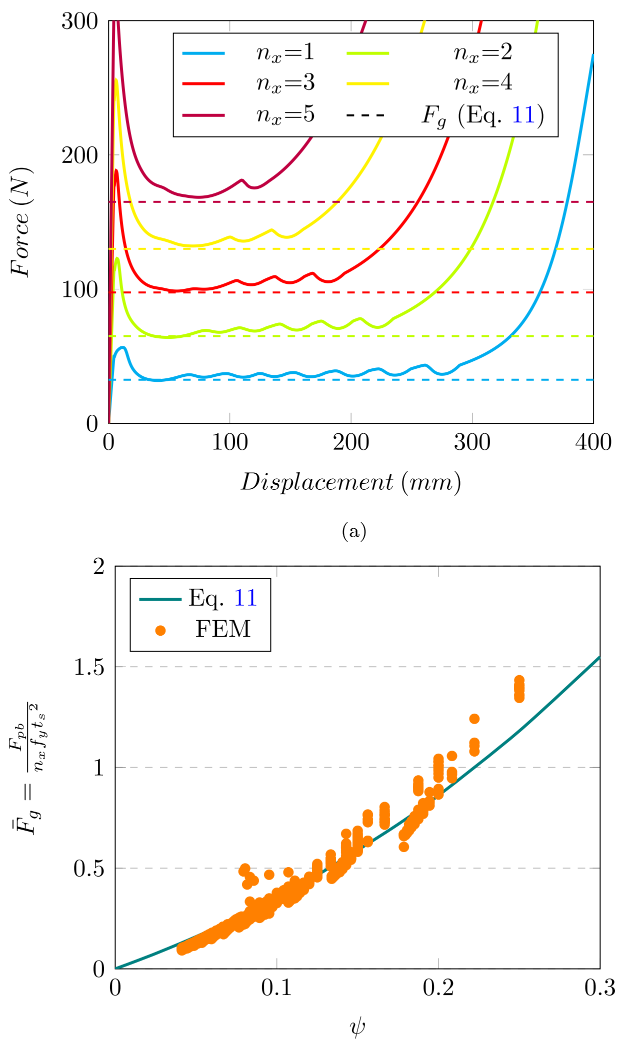

Fig. 12. (a) Force–displacement graphs from finite element analysis of specimen with L = 60 mm, w_h = 6 mm, L_y = 5 mm, n_y = 10, t_s = 1 mm and n_x = 1, 2, 3, 4 and 5 compared to the global force to propagate deformation along a ribbon Kirigami sheet, F_g, (Eq. (11)) shown as dashed lines. (b) Plot of the dimensionless global propagation force, $\bar{F}_g$, computed using Eq. (11) for $0.04 \leq \psi \leq 0.25$ and compared to finite element analysis showing good agreement.

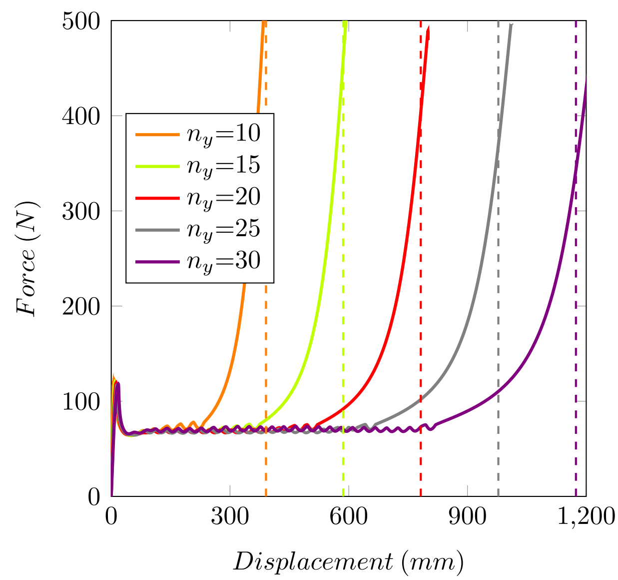

Fig. 13. Force–displacement plots obtained from finite element analysis for L = 60 mm, w_h = 6 mm, L_y = 5 mm, n_x = 2 and t_s = 1 mm with n_y = 10, 15, 20, 25 and 30 compared to the kinematic maximum extension (Eq. (12)) shown as dashed lines.

to ψ = 0.25 and thicknesses ranging from 0.6 to 1.2 mm. The results of the parametric study are plotted in dimensionless form in Fig. 12(b) showing good agreement with Eq. (11). To obtain F_g from finite element analysis the minimum force between Δ_2 and Δ_3 (see Fig. 11) was used.

To compute the maximum global displacement, Δ_{max}, we assume all unit cells along the length are at their maximum extension, $\delta_{max} = 2L_y\epsilon_{max}$, and multiply this by the number of unit cells in series, n_y:

$$\Delta_{max} = n_y\delta_{max} = n_y L_y \left(\frac{\sqrt{4\psi^2 + 1}}{\psi} - 2 \right) \tag{12}$$

Note that this neglects the influence of boundary conditions. It can be observed in Fig. 12(a) that as the number of unit cells across the width (n_x) increases, while keeping n_y the same, the stretching capacity gradually decreases. This reduction in stretching capacity is due to the boundary conditions imposed by the top and bottom grips. Therefore, for Eq. (12) to be accurate the ratio n_y/n_x should be sufficiently large to minimise the influence of the boundary conditions.

In Fig. 13 Δ_{max}, shown by the dashed lines, is compared to finite element analysis. Eq. (12) provides a good estimate of the ultimate stretching capacity of the Kirigami sheet.

The energy dissipated by the extension of the Kirigami sheet can finally be computed. By assuming the area $A_2 \geq A_1$, as shown in Fig.

11(b), the shaded rectangular area ($F_g \cdot \Delta_{\max}$) in Fig. 11(a) represents a lower bound on the maximum total energy dissipated by the Kirigami sheet. In dimensionless form, the maximum energy dissipated is:

$$\bar{U}_g = \frac{U_g}{n_x n_y f_y L_y {t_s}^2} = \frac{F_g \Delta_{max}}{n_x n_y f_y L_y {t_s}^2} = 2\bar{F}_{pb}\epsilon_{max}$$
$$= 2\pi\psi\left(2\psi + \sqrt{1+4\psi^2}\right)\left(\frac{\sqrt{4\psi^2+1}}{2\psi} - 1\right) = \pi \qquad (13)$$

For the design of an energy dissipating device there are three key parameters: the plateau load, F_g, given by Eq. (11); the maximum extension, Δ_{max}, given by Eq. (12); and the energy dissipation requirement, U_g, given by Eq. (13). A design must balance these parameters to meet the system requirements. The analysis presented above is compiled into a design methodology in the next section, followed by an example of its use for the design of a fall arrest system.

5. Design process for metallic ribbon Kirigami

For design the application requirements consist of a minimum energy dissipation requirement, U_{req}, a maximum arrest force (maximum force transmitted across the device), F_{req}, and a maximum extension, $\Delta_{max,req}$. The displacement demand, ρ, is obtained by taking the ratio of the energy dissipation requirement, U_{req}, and the required arrest force F_{req}. We then set this equal to the maximum global displacement (Eq. (12)):

$$\rho = \frac{U_{\rm req}}{F_{\rm req}} = n_y L_y\left(\frac{\sqrt{4\psi^2+1}}{\psi} - 2\right) \le \Delta_{max,req} \qquad (14)$$

If $\rho > \Delta_{max,req}$ the application requirements must be reviewed because a device which meets all three requirements is not possible. Taking the undeformed length of the device as $L_0 = 2n_y L_y$ and solving Eq. (14) for ψ we obtain:

$$\psi_{req} = \frac{L_0}{2\sqrt{2L_0\rho + \rho^2}} < \frac{2}{3} \qquad (15)$$

Thus by choosing an undeformed length, L_0, and using the energy and arrest force requirements, we obtain the required ψ.

By selecting the material yield stress, f_y, and plate thickness, t_s, the required number of unit cells across the width, n_x, is calculated using Eq. (11) by setting $F_{req} = F_g$:

$$(n_x)_{req} = \frac{F_{\rm req}}{\pi f_y t_s^2 \psi\left(2\psi + \sqrt{1+4\psi^2}\right)} \qquad (16)$$

Note that the system can consist of multiple layers, with layers arranged parallel to each other. For example, if $(n_x)_{\rm req} = 4$ two layers with $n_x = 2$ could be used instead of a single layer with $n_x = 4$. This does not have an effect on the analytical model predictions since the behaviour varies linearly with n_x.

A total cross-sectional area of $n_x w_h t_s$ links each row of unit cells. The link width, w_h must be selected to ensure the Kirigami does not yield before the arrest force is reached:

$$w_h > \frac{F_{req}}{f_y t_s n_x} \qquad (17)$$

It is desirable to take w_h significantly larger than the minimum value to improve robustness. Since we now have w_h and ψ_{req}, L_y is obtained from the definition $\psi = L_y/(L - 2w_h)$ by choosing the unit cell width $L = L_x + w_h$:

$$L_y = \psi_{req}(L - 2w_h) \qquad (18)$$

Finally, since $L_0 = 2n_y L_y$ the required number of rows is:

$$(n_y)_{req} = \frac{L_0}{2L_y} \qquad (19)$$

and all the key system parameters have now been determined. The design approach is summarised in Fig. 14. This approach is now applied to the design of a fall arrest system.

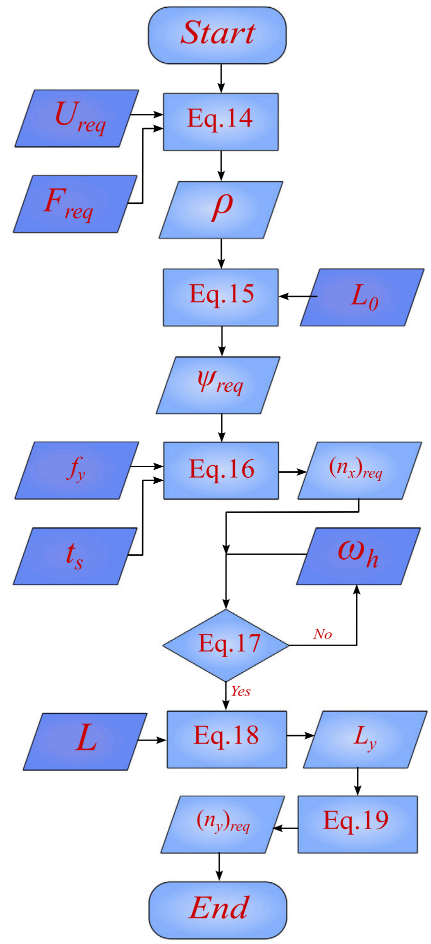

Fig. 14. Flowchart for the design of ribbon Kirigami-based tension energy-dissipating devices.

6. Design of a fall arrest system

Falls from height are the largest contributor to injuries and fatalities in the construction industry [37]. To address this the use of personal fall arrest systems is required in situations where falls cannot be prevented through other means [38]. In this section, we design a fall arrest system in accordance with BS EN 363 [39], BS EN 364 [40], and BS EN 355 [41] to practically demonstrate use of the proposed design methodology.

According to BS EN 364, the system must be capable of absorbing the energy of a 100 kg mass dropped from a height of 4 m, which translates to an energy dissipation requirement of $U_{req} = 3924J$. The maximum arrest force specified by BS EN 363 is 6000 N. However, $F_{req} = 5000$ N is used to provide a margin for variation in the properties of the device.

Using Eq. (14), the displacement demand:

$$\rho = \frac{3924}{5000} \approx 785 \text{ mm} \qquad (20)$$

We choose the initial device length of $L_0 = 300$ mm. Using Eq. (15) we find the required ψ:

$$\psi_{req} = \frac{125}{2\sqrt{188679}} \approx 0.144 < \frac{2}{3} \qquad (21)$$

According to BS EN 355 the maximum extension $\Delta_{max,req} = 2L_0$+1.75 m. The displacement condition in Eq. (14): $\rho = \frac{3924}{5000} < 2(300) + 1750 = 2350$ mm; therefore the system is viable.

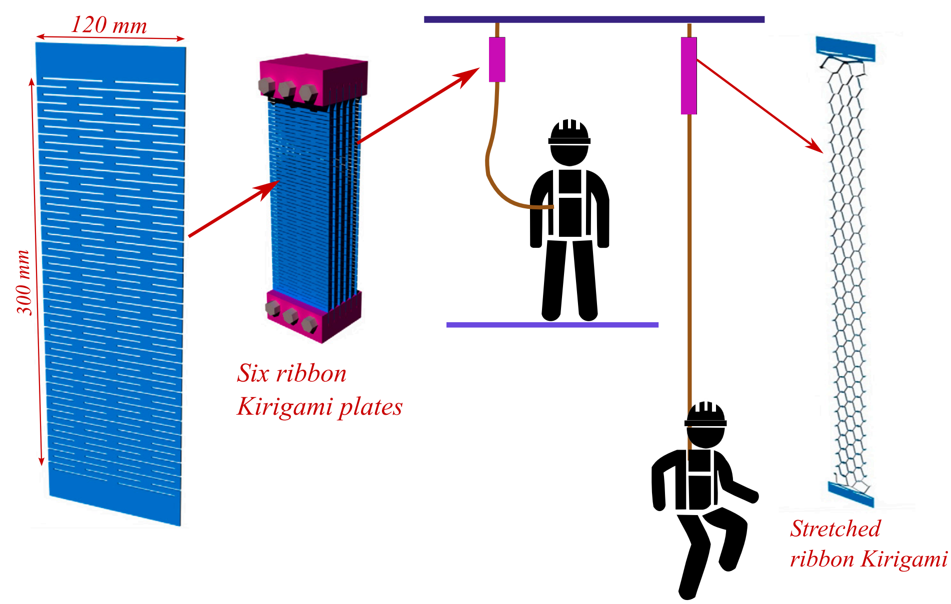

Fig. 15. Schematic drawing of the proposed fall arrest system energy absorber.

For this application we select a mild steel plate with a yield stress $f_y = 355$ MPa and thickness $t_s = 1.4$ mm. The required number of unit cells across the width, $(n_x)_{req}$, is obtained using Eq. (16):

$$(n_x)_{\mathrm{req}} = \frac{F_{\mathrm{req}}}{\pi f_y t_s^2 \psi \left(2\psi + \sqrt{1+4\psi^2}\right)} \approx 12 \tag{22}$$

Six layers with $n_x = 2$ are selected, as shown in Fig. 15.

According to Eq. (22), w_h must be sufficient to ensure that the total cross-sectional area of the links can transfer the force between the rows. Therefore,

$$w_h > \frac{5000}{355 \times 1.4 \times 2} = \frac{2500}{497} \approx 5 \text{ mm} \tag{23}$$

However, instead of 5 mm, a width of $w_h = 10$ mm is selected, resulting in links that are twice as strong for force transfer improving robustness.

An overall device width of $W = 120$ mm is chosen. With the selection of six layers and $n_x = 2$, the unit cell width is given as $L = W/n_x = 60$ mm. The parallel cut spacing, L_y, can now be calculated from Eq. (18):

$$L_y = \psi \left(L - 2w_h\right) \approx 5.7 \text{ mm} \tag{24}$$

Finally, the required number of rows is obtained using Eq. (19):

$$(n_y)_{req} = \frac{300}{2(5.7)} \approx 27 \tag{25}$$

To summarise all design parameters: $L_y = 5.7$ mm, $n_y = 27$, $n_x = 2$ (two layers), $L = 60$ mm, $w_h = 10$ mm, $f_y = 355$ MPa, $t_s = 1.4$ mm, and $L_x = L - w_h = 50$ mm. The proposed fall arrest system energy absorber is shown in Fig. 15.

The predicted force–displacement behaviour for one layer of the designed fall arrest system, characterised by the maximum displacement $\Delta_{\max}$ and arrest force F_g defined in Eqs. (11) and (12) respectively, is depicted by the dashed lines in Fig. 16. This is compared to a non-linear static finite element analysis showing good agreement.

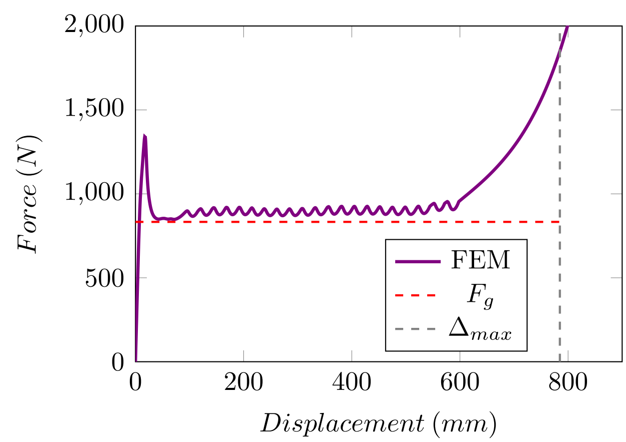

Fig. 16. Predicted force–displacement behaviour of one layer of the designed fall arrest system compared to finite element analysis showing good agreement.

7. Conclusions

In this study Kirigami techniques were used as the basis for metallic energy dissipating devices acting in tension. The ribbon Kirigami pattern, in the anti-symmetric deformation mode, was used due to its ability to accommodate extremely large strains. This unique characteristic makes it ideal for use as a tensile energy-absorbing device. The behaviour of metallic ribbon kirigami was characterised using a combination of reduced-order analytical modelling, a finite element analysis parametric study, and experimental validation, all showing very good agreement. Findings reveal that the behaviour of metallic ribbon Kirigami is governed by a single dimensionless parameter, ψ, which is related to the geometry of the unit cell.

A straightforward design methodology was proposed which produces the device geometry and cut pattern which meets specified requirements for the total energy dissipated, force transmitted through the device, and maximum extension. As a case study the methodology was applied to the design of a fall arrest system energy absorber. Metallic kirigami offers a simple and versatile method to manufacture tensile energy dissipating devices with a wide range of applications.

CRediT authorship contribution statement

Sahand Khalilzadehtabrizi: Writing – review & editing, Writing – original draft, Methodology, Investigation, Formal analysis, Data curation, Conceptualization. **Iman Mohagheghian:** Writing – review & editing, Supervision, Resources, Project administration, Methodology, Conceptualization. **Martin G. Walker:** Writing – review & editing, Supervision, Project administration, Methodology, Funding acquisition, Formal analysis, Conceptualization.

Declaration of competing interest

The authors declare the following financial interests/personal relationships which may be considered as potential competing interests: Martin Walker reports financial support was provided by the Engineering and Physical Sciences Research Council. If there are other authors, they declare that they have no known competing financial interests or personal relationships that could have appeared to influence the work reported in this paper.

Acknowledgements

This work was supported by the Engineering and Physical Sciences Research Council, United Kingdom [EP/X040666/2].

Data availability

Data will be made available on request.

References

[1] Midori Isobe, Ko Okumura, Initial rigid response and softening transition of highly stretchable kirigami sheet materials, Sci. Rep. 6 (1) (2016) 24758.
[2] Yue Sun, Wangjie Ye, Yao Chen, Weiying Fan, Jian Feng, Pooya Sareh, Geometric design classification of kirigami-inspired metastructures and metamaterials, in: Structures, vol. 33, Elsevier, 2021, pp. 3633–3643.
[3] Yigil Cho, Joong-Ho Shin, Avelino Costa, Tae Ann Kim, Valentin Kunin, Ju Li, Su Yeon Lee, Shu Yang, Heung Nam Han, In-Suk Choi, et al., Engineering the shape and structure of materials by fractal cut, Proc. Natl. Acad. Sci. 111 (49) (2014) 17390–17395.
[4] Yichao Tang, Jie Yin, Design of cut unit geometry in hierarchical kirigami-based auxetic metamaterials for high stretchability and compressibility, Extrem. Mech. Lett. 12 (2017) 77–85.
[5] Yi Yang, Marcelo A. Dias, Douglas P. Holmes, Multistable kirigami for tunable architected materials, Phys. Rev. Mater. 2 (11) (2018) 110601.
[6] Jean-François Sadoc, Jean Charvolin, Nicolas Rivier, Phyllotaxis on surfaces of constant Gaussian curvature, J. Phys. A 46 (29) (2013) 295202.
[7] J.-F. Sadoc, Nicolas Rivier, Jean Charvolin, Phyllotaxis: A non-conventional crystalline solution to packing efficiency in situations with radial symmetry, Acta Crystallogr. Sect. A 68 (4) (2012) 470–483.
[8] Maryam Eidini, Glaucio H. Paulino, Unraveling metamaterial properties in zigzag-base folded sheets, Sci. Adv. 1 (8) (2015) e1500224.
[9] Xingjian Li, Yijie Gai, Maocheng Sun, Yinwen Li, Shoufang Xu, Drum tower-inspired kirigami structures for rapid fabrication of multifunctional shape-memory smart devices with complex and rigid 3D geometry in a two-stage photopolymer, Adv. Funct. Mater. 32 (40) (2022) 2205842.
[10] Taiju Yoneda, Yoshinobu Miyamoto, Hirofumi Wada, Structure, design, and mechanics of a pop-up origami with cuts, Phys. Rev. Appl. 17 (2) (2022).
[11] Isabel M. de Oliveira, Eduardo M. Sosa, Emily Baker, Sigrid Adriaenssens, Experimental and numerical investigation of a rotational kirigami system, Thin-Walled Struct. 192 (2023) 111123.
[12] Xingjian Li, Lele Wang, Yinwen Li, Shoufang Xu, Reprocessable, self-healing, thermadapt shape memory polycaprolactone via robust ester–ester interchanges toward kirigami-tailored 4D medical devices, ACS Appl. Polym. Mater. 5 (2) (2023) 1585–1595.
[13] Ye Xue, Zihan Wang, Ankan Dutta, Xue Chen, Peng Gao, Runze Li, Jiayi Yan, Guangyu Niu, Ya Wang, Shuaijie Du, et al., Superhydrophobic, stretchable kirigami pencil-on-paper multifunctional device platform, Chem. Eng. J. 465 (2023) 142774.
[14] Lung Chow, Guangyao Zhao, Pengcheng Wu, Xingcan Huang, Jiyu Li, Jian Li, Wanying Wang, Guihuan Guo, Zhiyuan Li, Jiachen Wang, Jingkun Zhou, Yawen Yang, Yuyu Gao, Binbin Zhang, Qiang Zhang, Dengfeng Li, Ya Huang, Kuanming Yao, Jian Lu, Xinge Yu, Soft, body conformable electronics for thermoregulation enabled by kirigami, Bio- Des. Manuf. 7 (4) (2024) 453–462.
[15] Ahmad Rafsanjani, Lishuai Jin, Bolei Deng, Katia Bertoldi, Propagation of pop ups in kirigami shells, Proc. Natl. Acad. Sci. 116 (17) (2019) 8200–8205.
[16] Martin G. Walker, Folding auxetic polygonal kirigami tubes, J. Mech. Robot. 16 (12) (2024) 121012.
[17] Yun Kyu Yi, Jie Yin, Yichao Tang, Developing an advanced daylight model for building energy tool to simulate dynamic shading device, Sol. Energy 163 (2018) 140–149.
[18] Rodrigo Arauz, Aminallah Pourasghar, John C. Brigham, Evaluation of the effects of cut design parameters on the environmental performance of a kirigami-inspired façade concept, Energy Build. 297 (2023) 113432.
[19] Shanpeng Li, Jingxin Zhu, Cong Liu, Ruihua Zhang, Jianlin Liu, Zhiguang Guo, Load-responsive bionic kirigami structures for high-efficient fog harvesting, Chem. Eng. J. 464 (2023) 142549.
[20] Aaron Lamoureux, Kyusang Lee, Matthew Shlian, Stephen R. Forrest, Max Shtein, Dynamic kirigami structures for integrated solar tracking, Nat. Commun. 6 (1) (2015) 8092.
[21] Erin E. Evke, Chao Huang, Yu-Wei Wu, Michael Arwashan, Byungjun Lee, Stephen R. Forrest, Max Shtein, Kirigami-based compliant mechanism for multiaxis optical tracking and energy-harvesting applications, Adv. Eng. Mater. 23 (4) (2021) 2001079.
[22] Wen Zhang, Jun Xu, Ultra-light kirigami lantern chain for superior impact mitigation, Extrem. Mech. Lett. 51 (2022) 101602.
[23] Tom Corrigan, Patrick Fleming, Charlie Eldredge, Delony Langer-Anderson, Strong conformable structure via tension activated kirigami, Commun. Mater. 4 (1) (2023) 31.
[24] Shizhao Ming, Caihua Zhou, Tong Li, Zhibo Song, Bo Wang, Energy absorption of thin-walled square tubes designed by kirigami approach, Int. J. Mech. Sci. 157–158 (2019) 150–164.
[25] Zhejian Li, Wensu Chen, Hong Hao, Qiusong Yang, Rui Fang, Energy absorption of kirigami modified corrugated structure, Thin-Walled Struct. 154 (2020) 106829.
[26] Jiayao Ma, Huaping Dai, Sibo Chai, Yan Chen, Energy absorption of sandwich structures with a kirigami-inspired pyramid foldcore under quasi-static compression and shear, Mater. Des. 206 (2021) 109808.
[27] Zhejian Li, Qiusong Yang, Rui Fang, Wensu Chen, Hong Hao, Crushing performances of kirigami modified honeycomb structure in three axial directions, Thin-Walled Struct. 160 (2021) 107365.
[28] Dassault Systèmes Simulia Corp, Abaqus/CAE 2022, 2022.
[29] Gordon R. Johnson, William H. Cook, A constitutive model and date for metals subject to large strains, high strain rates and high temperatures, in: Proceedings of the 7th International Symposium on Ballistics, the Hague, Netherlands, 1983.
[30] Juyong Cao, Jun Zhang, Yanfeng Xing, Fuyong Yang, Xiaobing Zhang, Peiyun Xia, Xiaoyu Ma, Experimental and numerical investigation of a novel pinless friction stir spot welding for Al 1060 sheets, Int. J. Adv. Manuf. Technol. (2024) 1–10.
[31] B.K.J. Hiriyur, B.W. Schafer, Yield-line analysis of cold-formed steel members, Int. J. Steel Struct. 5 (1) (2005) 43–54.
[32] K.A. Seffen, S. Pellegrino, Deployment dynamics of tape springs, Proc. R. Soc. Lond. Ser. A Math. Phys. Eng. Sci. 455 (1983) (1999) 1003–1048.
[33] Martin G. Walker, Keith A. Seffen, The flexural mechanics of creased thin strips, Int. J. Solids Struct. 167 (2019) 192–201.
[34] Lorna J. Gibson, Michael F. Ashby, Cellular solids: Structure and properties, second edition, 2014, pp. 1–510,
[35] Souhayl Sadik, Martin G. Walker, Marcelo A. Dias, On local kirigami mechanics II: Stretchable creased solutions, J. Mech. Phys. Solids 161 (2022) 104812.
[36] Stelios Kyriakides, in: John W. Hutchinson, Theodore Y. Wu (Eds.), Propagating Instabilities in Structures, in: Advances in Applied Mechanics, vol. 30, Elsevier, 1993, pp. 67–189.
[37] Xinyu Huang, Jimmie Hinze, Analysis of construction worker fall accidents, J. Constr. Eng. Manag. 129 (3) (2003) 262–271.
[38] H.M. Government, Work at height regulations 2005, 2005, https://www.legislation.gov.uk/uksi/2005/735.
[39] European Committee for Standardization, Personal Fall Protection Equipment - Personal Fall Protection Systems, BS EN 363:2018, British Standards Institution, Brussels, Belgium, 2018.
[40] European Committee for Standardization, Personal Protective Equipment Against Falls from a Height – Test Methods, BS EN 364:1993, British Standards Institution, Brussels, Belgium, 1993.
[41] European Committee for Standardization, Personal Protective Equipment Against Falls from a Height - Energy Absorbers, BS EN 355:2002, The British Standards Institution, Brussels, Belgium, 2002.